DISCLAIMER

This report was prepared as an account of work sponsored by an agency of the United States Government. Neither the United States Government nor any agency thereof, nor any of their employees, makes any warranty, express or implied, or assumes any legal liability or responsibility for the accuracy, completeness, or usefulness of any information, apparatus, product, or process disclosed, or represents that its use would not infringe privately owned rights. Reference herein to any specific commercial product, process, or service by trade name, trademark, manufacturer, or otherwise does not necessarily constitute or imply its endorsement, recommendation, or favoring by the United States Government or any agency thereof. The views and opinions of authors expressed herein do not necessarily state or reflect those of the United States Government or any agency thereof. Reference herein to any social initiative (including but not limited to Diversity, Equity, and Inclusion (DEI); Community Benefits Plans (CBP); Justice 40; etc.) is made by the Author independent of any current requirement by the United States Government and does not constitute or imply endorsement, recommendation, or support by the United States Government or any agency thereof.

SAND2025-13931R

Grant or Contract Number: N0001424IP00028-Sandia Proposal 018200129
Date Prepared: 10/8/2025
Project Title: Development of Metal Boride/Carbide Precursors for MOCVD Applications
Annual Summary Report: CY2025
Principle Investigator: Harrison D. Root, 505-537-2448, hdroot@sandia.gov; Sandia National Laboratories

Major Goals:

The goal of this program is to develop tailored precursors that can be used for MOCVD processes to produce intercalated thermal protective coatings of metal borides (MB_x), and metal carbides (MC_y). The approach is to: (1) use molecular modeling to identify potential candidate precursors, (2) synthesize existing and new precursors, and (3) evaluate all precursors by MOCVD to produce MB_x and MC_y films and coatings. The objectives for this three-year program include: *Year 1*: Synthesize/obtain precursors with initial evaluation; *Year 2*: Verify Precursor Utility Under CVD Conditions; and *Year 3*: Optimization of volatility, purity, and quality of final films. Results are anticipated to overcome the limitations of commercial/state-of-the-art precursors used in vapor processing.

Accomplished:

This report describes the efforts for calendar year (CY) 2025 to develop refractory metal boride/carbide precursors that can be processed by metal-organic chemical vapor deposition (MOCVD) processing techniques. During CY25, our team has used density-functional theory (DFT) modeling to explore mechanistic pathways for the decomposition of bis(cyclopentadienyl) zirconium (zirconocene) derivatives. Zirconocene precursor ligand modifications impact decomposition energies *en-route* to a key dialkene-zirconium adduct, which is presumed to further decompose to ZrC phases. Bulkier ligand sets lower the decomposition energies in this mechanism by 10s of kJ/mol *via* stabilization of intermediate species, which results in more favorable decomposition to ZrC phases. Furthermore, experimental MOCVD processing of commercially available and custom synthesized zirconocene (and hafnocene) has demonstrated not only material transfer, but changes in precursor volatility and final quality of the ceramic product. Further effort over the remaining timeline will focus on additional evaluation of the resultant films *via* X-ray photoelectron spectroscopy (XPS) to determine the degree of oxygen contamination, as well as degree of amorphous carbon present in the final product. Please see attached document for in-depth analysis and discussion of research activities this reporting period.

Training:

Nothing to report.

Dissemination:

Effect of Ligand Substitution for Zirconium Carbide Chemical Vapor Deposition (CVD), 2025 Rocky Mountain Regional Metting – Presentation

Christian, M. S.; Goodman-Miller, S. A.; Boissiere, J. D.; Root, H. D.; "Effects of Ligand Substitution for Zirconium Carbide Chemical Vapor Deposition (CVD)" *Manuscript in Preparation*

Plans:

- Finalize theoretical modeling manuscript.
- Continue optimization of precursor synthesis.
- Continued processing of custom precursors.
- Manuscript on synthesis and processing is in preparation.
- XPS analysis of the produced films to characterize film quality.
- Continued collaboration with Prof. Thomas Gray (Case Western) to process materials.

Honors:

Nothing to report.

Technology Transfer:

Precursors developed through this program will be compared to current state-of-the-art precursors employed by ONR for CVD processing by correlating binding energies and thermal properties. We will develop our transitions plan as candidates are determined.

Participants:

Harrison Root

Months Worked – 12

Jacob Boissiere

Months Worked – 12

Matthew Christian

Months Worked – 12

Sydnee Wall

Months Worked – 6

Sydney Goodman – Miller

Months Worked – 3

Brianna Addison

Months Worked – 6

Other Collaborators:

Professor Thomas Gray – Case Western Reserve University – Providing custom synthesized precursors for processing

Partners:

Case Western Reserve University

Thomas Gray collaborating on the project, funded independently.

Students:

3 students supported

1 student graduated during reporting period (Sydney Goodman-Miller)

Attached Report Below:

Synthesis and Processing:

Custom ceramic precursors were synthesized following modified literature procedures. We focused our efforts on varying alkyl groups that are directly bound to metals in bis(cyclopentadienyl) zirconium (IV) (or hafnium (IV)) materials (Figure 1). In a general synthesis, bis(cyclopentadienyl) zirconium (IV) chloride was mixed with 2.5 equivalents of an alkyl magnesium bromide in diethyl ether at room temperature for two hours. Following purification, the resultant alkyl zirconium species were recrystallized, and successful synthesis was determined by single crystal X-ray diffraction. Specific synthetic procedures are outlined below.

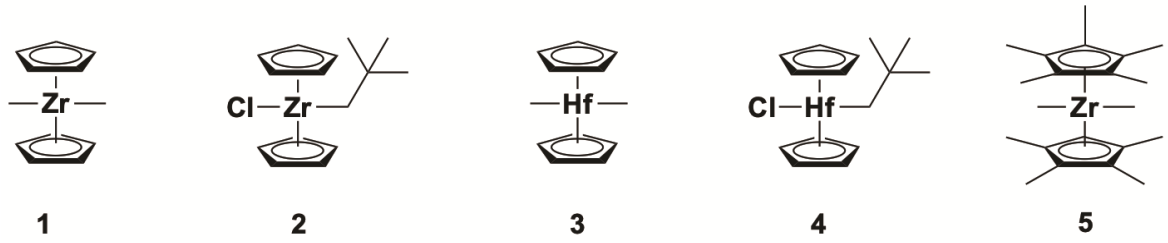

Figure 1. Custom synthesized Zr/Hf precursors.

*Dimethyl Bis (cyclopentadienyl) Zirconium (IV) (**1**)*

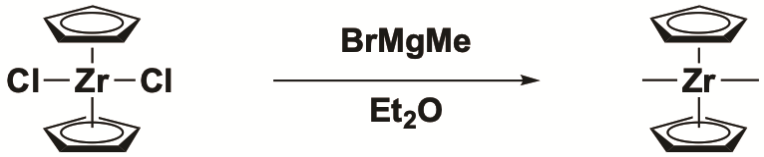

Scheme 1. Synthesis of **1**.

In a glovebox, a 250 mL round bottom flask was charged with 0.7797 g of bis(cyclopentadienyl) zirconium (IV) dichloride and 80 mL of diethyl ether. The solution was stirred, and 0.48 mL of 3.0 M methyl magnesium chloride (in THF) was added dropwise. The solution was allowed to stir at room temperature for two hours. After the reaction was completed, the solvent was removed under vacuum and the resultant powder dissolved in 50 mL of toluene. The resulting solution was filtered through celite and the solvent again removed under vacuum to result in a powder product. This powder was dissolved in 50 mL of pentane, filtered through a glass frit and then the solvent was removed. The white solid was recrystallized in pentane at – 30 °C to result in **1**.

*Dimethyl Bis(cyclopentadienyl) Hafnium (IV) (**2**)*

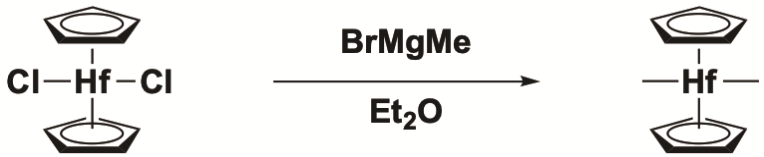

Scheme 2. Synthesis of **2**.

The same protocol used to synthesize **1** was used here.

*Neopentyl Bis(cyclopentadienyl) Zirconium (IV) Chloride (**3**)*

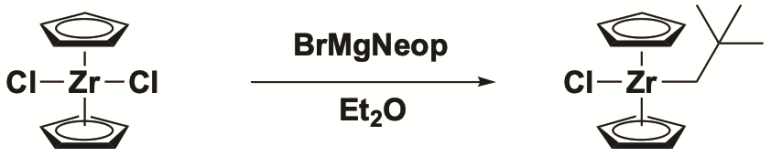

Scheme 3. Synthesis of **3**.

The same protocol used to synthesize **1** was used here.

*Neopentyl Bis(cyclopentadienyl) Hafnium (IV) Chloride (**4**)*

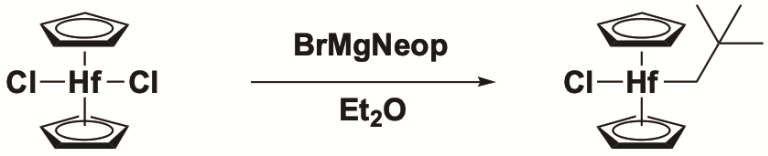

Scheme 4. Synthesis of **3**.

The same protocol used to synthesize **1** was used here.

The successful syntheses of **1** – **4** was demonstrated via single crystal X–ray diffraction (Figure 2). Structures determined from recrystallizing precursors **1** – **4** in pentane match expected structures and also demonstrated that Hf/Zr structures containing analogous ligands are in fact isostructural.

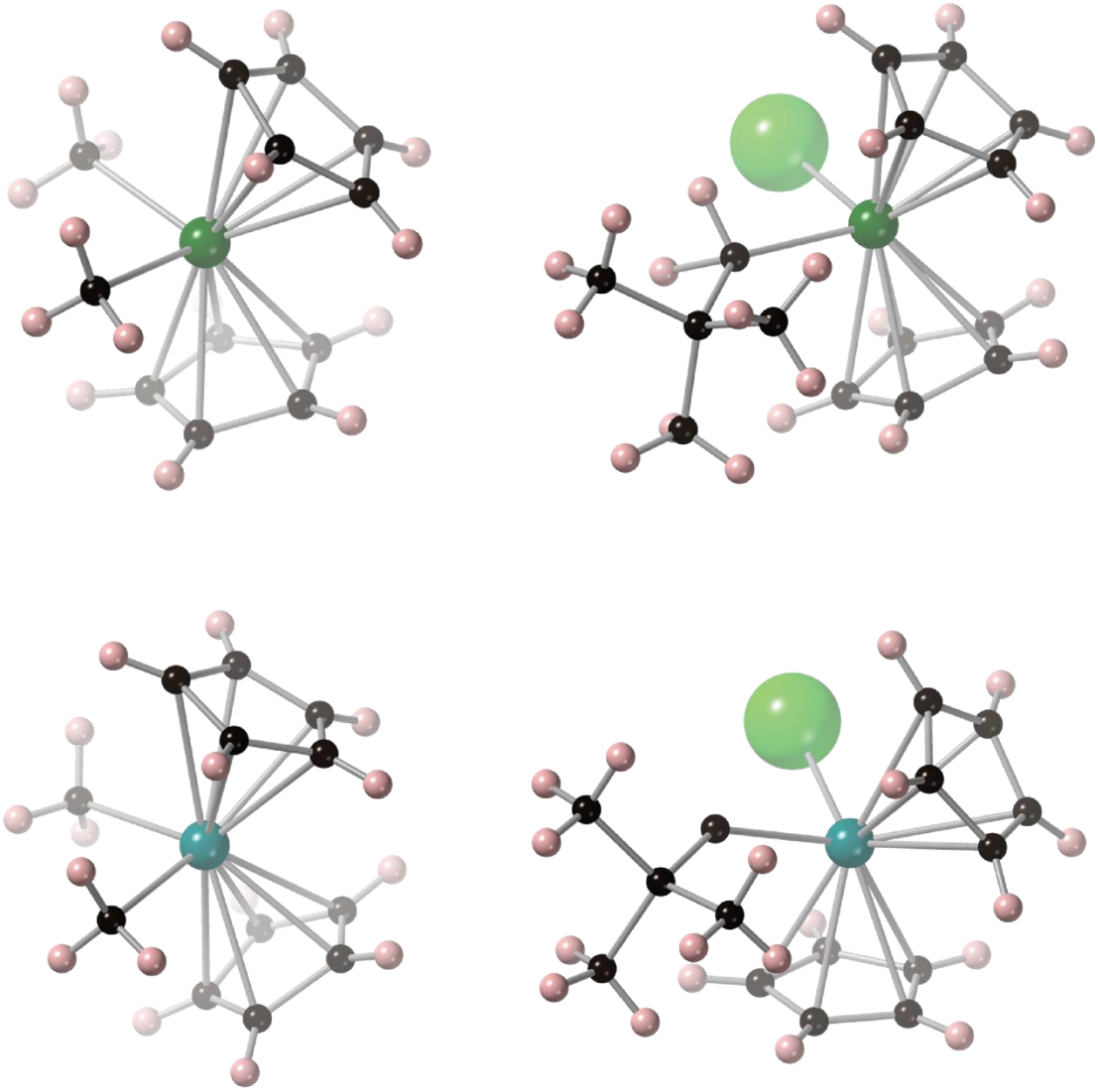

Figure 2. Representation of metal-organic compound structures of **1** – **4** determined using single crystal X-ray diffraction.

In addition to the custom synthesized precursors, commercial precursors were also evaluated for MOCVD processing to group IV carbides. Namely, dimethyl bis(pentamethylcyclopentadienyl) zirconium (IV) (referenced as compound **5**) was used to explore the impact of methyl substitution on the Cp ring. This material was purchased from Sigma Aldrich and used as received without further purification.

Metal - Organic Chemical Vapor Deposition Processing (MOCVD)

Custom synthesized (**1**, **3**) and commercially available (**5**) ceramic precursors were processed using MOCVD in a custom-built processing system (Figure 3). All materials were processed under an active vacuum with a flowing gas of 3% hydrogen in argon mixture. Solid samples were inertly loaded into the processing equipment and heated to 200 – 250 °C. The processing zone of the furnace was heated at 20 °C/min and then maintained at 900 °C for 8 hours. Silica wafer substrates were placed along the furnace processing zone, to capture any materials which deposited at different locations.

Figure 3. Custom built MOCVD system used herein.

Both **1** and **3** were able to be effectively processed using an MOCVD approach. Substrates collected from processing **1** showed substantial material deposition onto the silica substrate. Scanning electron microscope (SEM) imaging showed a variety of material morphologies in the deposited product, including film – like sections, and more complex ribbons. Importantly, energy – dispersive X-ray spectroscopy (EDS) revealed that the deposited product contains a large amount of Zirconium (Figure 4). Additional signals were observed for both oxygen and carbon, as well as silicon (which arises from the substrate). Mapping of the EDS revealed that the features observed are primarily zirconium and carbon based, with relatively minimal contamination from oxygen (Figure 4). Notably, there is no chloride observed by EDS, further indicating successful substitution of the chloride present in the starting material.

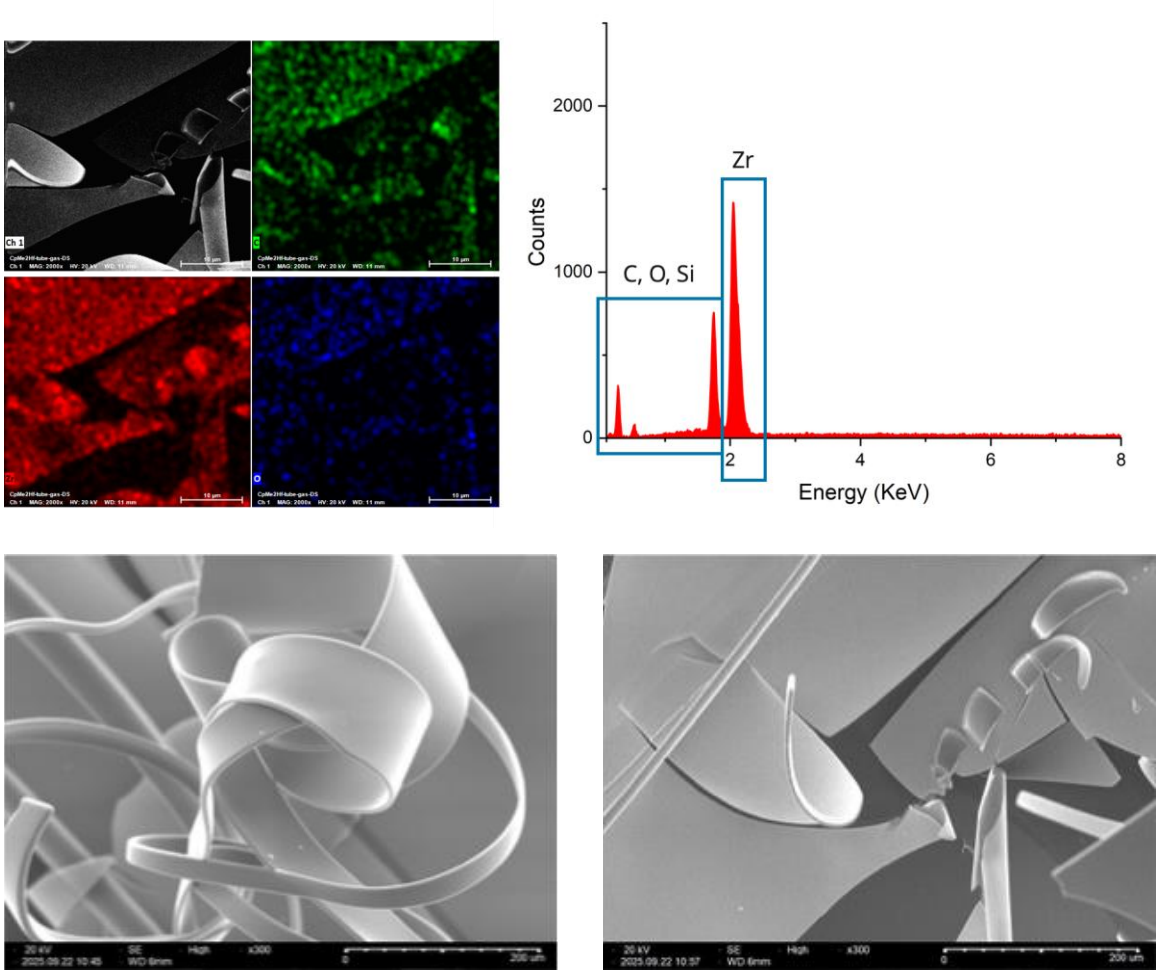

Figure 4. EDS mapping, spectra and SEM imaging of material resulting from processing of **1**.

Processing of **3** *via* the same conditions outlined above also resulted in the deposition of material onto the silicon substrates. Qualitatively, there was less material deposited from the processing of **3** than there was of **1**, and further analysis is underway to quantify this difference as well as understand why this could be. Substrates harvested from the processing of **3** also displayed a variety of morphologies in the final product when subjected to SEM analysis. These ranged from flakes to ribbons and EDS analysis on these product features showed deposition of hafnium, with smaller contributions of carbon and oxygen in the EDS spectra (Figure 5). Interestingly, it was observed in EDS that a higher ratio of oxygen is present in the product resulting from **3** than there was for **1**. Due to the nature of the thin films which were deposited, powder X-ray diffraction analysis proved inconclusive in identifying the exact phase of product. As such, further analysis is to be carried out using XPS to determine the quality of the carbide product, as well as identify any side products which were formed. Interestingly, processing commercial material **5** did not result in efficient material transfer under the conditions noted above, and precursor sublimation and transfer did not occur under varying conditions without resulting in decomposition of **5**. The lack of material deposition demonstrates how modification of the ligand set can have a profound impact on precursor volatilization and subsequent film deposition.

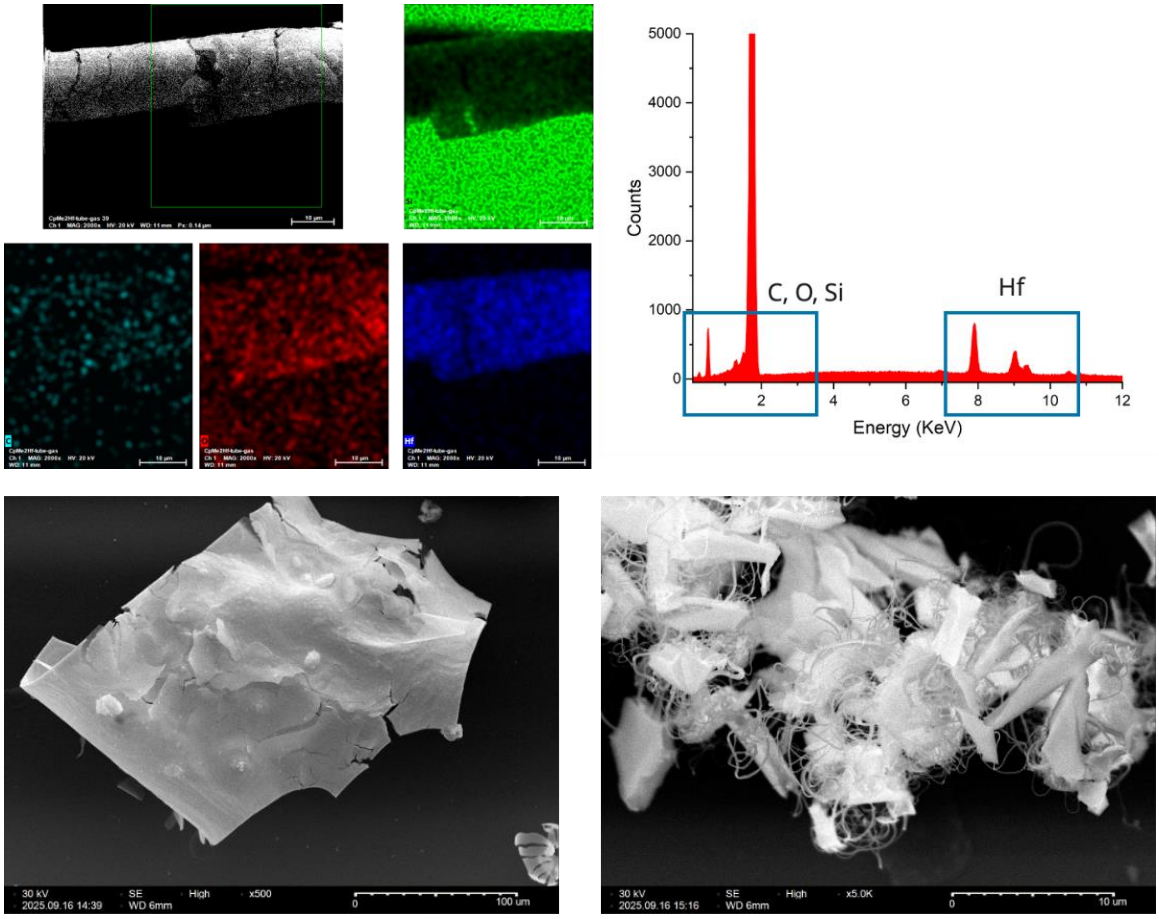

Figure 5. EDS mapping, spectra and SEM imaging of material resulting from processing of **3**.

In addition to the custom built MOCVD furnace, which was used for the processing above, new MOCVD capability has been procured and is shown in Figure 6. Our team has purchased a plasma – enhanced MOCVD system (PE-MOCVD). With this new system, we can process materials at sub-ambient pressures with a 3-gas mixing system with controlled flowrates, and up to temperatures of 1700 °C. An in-line induction coil can produce a plasma in the carrier gas, enabling further processing control and modification, which will assist in material volatilization and decomposition to ensure efficient material transfer. With this added capability, we will have the capacity to fine tune our processing conditions and allow for optimization of thin film formation.

Figure 6. Commercial plasma enhanced MOCVD system procured during this funding period, with the induction coil shown on the left. Temperature control is shown on the furnace body, and not-pictured is the gas-mixing module, vacuum system, and AC power controller for the plasma generation system.

Molecular Modeling

We used DFT computational modeling to explore how zirconocene ligand modification affects alpha hydride elimination reaction energies to form dialkene-zirconium. Zirconocene complexes (Figure 7) were systematically varied in size and functional group. The findings indicate that increasing the ligand size decreases the first alpha-hydride elimination reaction energy, suggesting that larger ligands may facilitate the approach of reactants or stabilize certain transition states, thereby lowering the energy barrier for the reaction. However, this effect is counterbalanced by an increase in the second alpha-hydride elimination reaction energy. Functional group and ligand size modifications all impacted the energetics of the alpha hydride elimination reaction, providing insights for the rational design of more efficient ZrC CVD precursors.

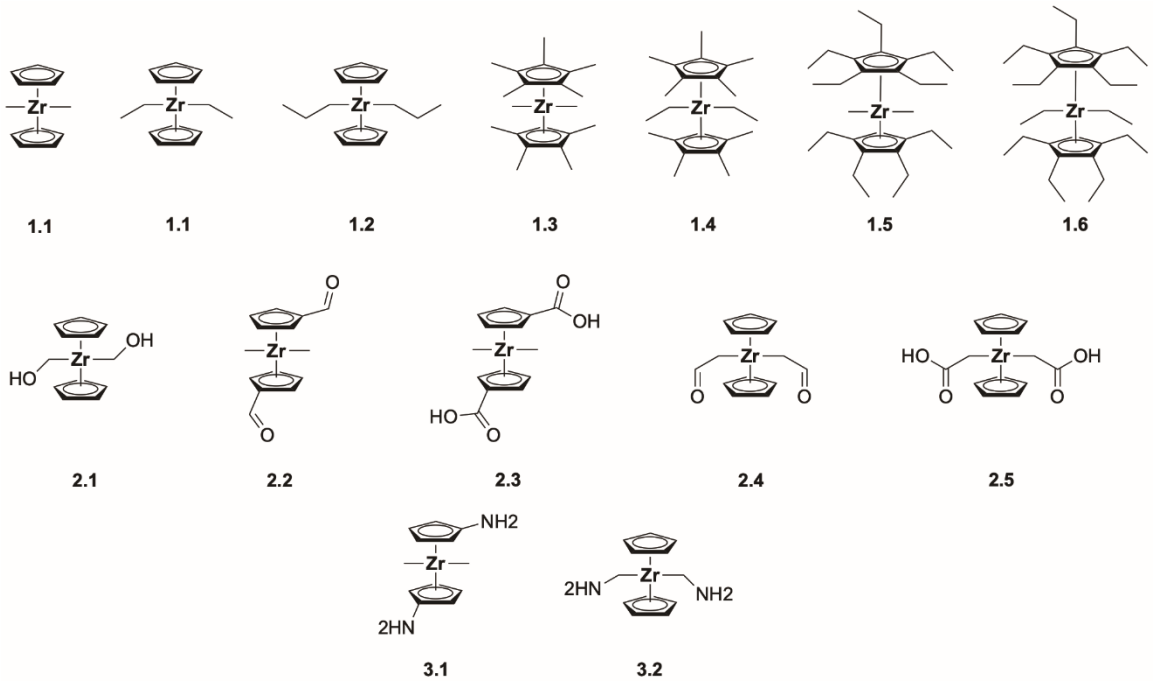

Figure 7. Zirconocenes investigated herein structures follow the numbering convention (class.number).

All calculations were performed using the Fritz Haber Ab Initio Materials Simulator (FHI-AIMS).[1-4] Each calculation used the B3LYP exchange-correlation functional,[5] and the exchange-hole dipole moment (XDM)[6,7,8] van der Waals correction. Relativistic scalar ZORA[9] corrections were also included in each calculation. The energy convergence criterion was set to 1×10−4 eV. The "light" basis[10] functions were used, as previous studies have demonstrated their effectiveness in accurately modeling chemical reactions. Reaction energies were calculated using:

$$E_{DFT,RXN} = \sum E_{DFT,Prod} - \sum E_{DFT,React}$$

where $E_{DFT,RXN}$ is the DFT reaction energy, $E_{DFT,Prod}$ is the DFT energy for reaction product energies and $E_{DFT,React}$ is the DFT energy for the reaction molecules.

Dimethyl-zirconocene served as the foundational compound for our investigation into reaction mechanisms, meaning that decomposition energies are referenced to the energy of this molecule. We categorized the selected molecules into three distinct classes based on ligand type attached to the zirconocene framework. Class 1 contains alkyl substituents where we systematically varied the lengths of both the zirconium and Cp alkyl ligands. Specifically, the lengths of the Zr alkyl ligands were extended up to three carbon atoms, while the Cp ligands were examined with lengths of up to two carbon atoms. Class 2 contains oxygen-incorporated ligands, such as hydroxyl (-OH), aldehyde (-CHO), and carboxylic acid (-COOH) to either the alkyl or cyclopentadiene ligand. Class 3 contains primary amine additions to both the Cp and alkyl groups. The decomposition reactions of these modified zirconocenes are analyzed in two distinct steps, leading to the formation of a zirconium dialkene complex (Figure 8). Notably, zirconocene reactions that feature alkyl chain

lengths greater than one exhibit two possible reaction pathways, which we subsequently define using an alpha-numeric system for clarity and organization.

Finally, Bader charges for the optimized geometries of selected molecules were calculated to analyze the charge and charge transfer of the zirconocene complexes and their intermediate ligands. This analysis was conducted using the Critic2 software package.[11,12] By examining the Bader charges, we aim to elucidate the electronic interactions and charge redistribution that occur during the reaction processes.

Decomposition Energies

a)

b)

c)

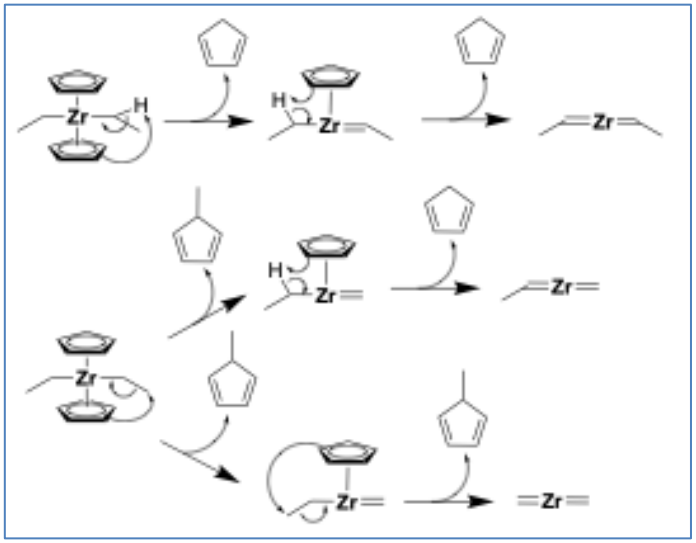

Figure 7. Illustration of reaction 1.2 and the three possible Zr hydride removal reactions. Reaction a) involves removal of Cp via hydrogenation, b) alkyl transfer to Cp followed by Cp hydrogenation, and c) alkyl transfer to Cp for both ligands.

Class	Number		ΔE_1 (kJ/mol)	ΔE_2 (kJ/mol)	$\Delta\Delta E_{Total}$
1	1		410	434	0
	2	a	373	453	-18
		b	404	422	-18
		c		416	-24
	3	a	371	454	-19
		b	408	420	-16
		c		419	-17
	4		404	436	-4
	5	a	374	419	-52
		b	336	450	-58
		c		436	-72
	6		382	444	-18
	7	a	366	417	-61
		b	335	447	-62
		c		439	-70
2	1		343	459	-42
	2		404	435	-5
	3		422	434	12
	4	a	335	587	78
		b	276	548	-20
		c		509	-59
3	1		400	431	-13
	2	a	338	445	-61
		b		435	-71

Table 1. Decomposition energies for different zirconocene ligand molecules. Class 1 contains alkyl ligands, class 2 contains -OH substituents, and class 3 contains -NH2 ligands.

Table 1 presents the decomposition reaction energies for all investigated zirconocene complexes (Figure 7) and shows $\Delta\Delta E_{Total}$ that is expressed in terms of the difference of the sum of ΔE_1 and ΔE_2 for the molecule and dimethyl-zirconium. For zirconocenes with methyl ligands, there is only one intermediate formed upon the removal of a Cp ligand, while zirconocenes with larger carbon chains

have two possible intermediates and three possible products that result from the elimination of a combination of the Cp ligand and alkyl groups. Our findings show a general trend where initial dissociation energies decrease as the size of the zirconocene ligands increases, indicating more favorable reaction pathways as the size of ligand is increased. This trend is attributed to the stabilization of the intermediates formed during the reaction. However, this stabilization comes at the cost of increased decomposition energy required for the formation of the final zirconium alkene product.

Reactions a-c for Class 1 investigated impact of alkyl ligand length on dissociation energies (Figure 7, and Appendix A. Figures 10 - 12). As the alkyl chain length increased from methyl to ethyl, we observed a significant reduction in the decomposition energy associated with the removal of the first Cp ligand, with a decrease of 30 kJ/mol. However, this increase in alkyl length resulted in a 19 kJ/mol increase in the decomposition energy for the removal of the second Cp ligand, leading to a net decrease of 11 kJ/mol in overall decomposition energy. However, dissociation energies in dipropyl zirconocene were only lowered by 2 and 1 kJ/mol compared to diethyl-zirconocene. Furthermore, both ethyl- and propyl-zirconocenes can yield dimethylzirconium through the formation of methyl- and ethyl-substituted Cp ligands (Appendix A. Figures 11 – 12. The decomposition energies for these pathways are notably lower, with reductions of 23 kJ/mol and 17 kJ/mol, respectively, compared to dimethyl zirconocene (**1**). Additionally, a third product can be formed from the ethyl- and propyl-ligand complexes, resulting in methyl-ethyl or methyl-propyl zirconium species. However, these products are less favored, exhibiting overall higher decomposition energies by 6 kJ/mol and 1 kJ/mol, respectively.

Adding methyl groups to the Cp ligand (commonly denoted as Cp*) results in a decrease in decomposition energy by 4 kJ/mol. Substitution of the methyls bound to Zr with ethyl groups (diethyl-Cp* zirconium) shows a minimal change on the energies required to generate diethylene zirconium, comparted to diethyl zirconocene (Appendix A. Figures 13 – 16). However, the formation of dimethyl-zirconium is significantly more favorable, exhibiting a decrease in decomposition energy of 72 kJ/mol relative to dimethyl zirconocene and 48 kJ/mol compared to diethyl-zirconocene. The transition from methyl to ethyl groups on the Cp ligand results in a smaller change in decomposition energy, yielding an overall stabilization of 8 kJ/mol. When ethyl is used as a ligand on both the Cp and zirconium, the only product formed is diethyl-zirconium (Appendix A. Figure 16. In this case, the preferred reaction pathway involves the insertion of a methyl group onto the Cp ligand, leading to the formation of a tertiary carbon. This pathway is energetically favorable, resulting in a decrease in energy of 52 kJ/mol.

Select mechanisms involving hydroxyl, aldehyde, and carboxylic acid functional groups are reported herein (Appendix A. Figures 17 – 20). The introduction of a hydroxyl group on the cyclopentadiene ligand in dimethyl zirconocene resulted in a reduction of the decomposition energy by 42 kJ/mol (Appendix A. Figure 17). Replacing the hydroxyl group with an aldehyde decreased the first decomposition step to as low as 276 kJ/mol (Appendix A. Figure 20). However, this modification resulted in a higher energy barrier for the second decomposition step, which rose to 509 kJ/mol. Overall, this change led to a net reduction of 59 kJ/mol in the formation energy of dimethyl-zirconium. This reaction pathway favored the formation of a di-aldehyde product over dimethylene zirconium. Furthermore, adding an aldehyde to the Cp ligand lowered the overall reaction energy by 5 kJ/mol. In contrast, the introduction of a carboxylic acid increased the decomposition energy by 12 kJ/mol. This increase can be attributed to the stabilizing effect of the carboxylic acid on the zirconocene complex, which raises the energy barrier for decomposition.

Two amine-containing analogues were investigated: $CpNH_2$ (aminocyclopentadiene) and methylamine (Appendix A. Figures 21, 22). The introduction of $CpNH_2$ resulted in a reduction of the decomposition energy for dimethyl-zirconium by 13 kJ/mol. In contrast, the methylamine ligand significantly lowered the decomposition energy by 63 kJ/mol, demonstrating a more pronounced effect on the reaction energetics. While methylamine facilitated the formation of dimethylzirconium, it also favored the formation of an alternative product, dimethylamine-zirconium, which exhibited a preferential decomposition enthalpy that was lower by 8 kJ/mol compared to the dimethyl-zirconium pathway.

Charge Transfer

Class	Number		Starting				ΔE_1(kJ /mol)	Intermediate				ΔE_2(kJ/ mol)
			Zr	C	C’	Cp $\bar{C}$		Zr	C	C’	Cp $\bar{C}$	
1	1		37.97	6.34	6.35	6.10	410	38.05	6.69	6.28	6.11	434
	2	a	37.98	6.32	6.31	6.10	373	38.13	6.64	6.35	6.11	453
		b					404	38.05	6.66	6.42	6.12	422/416
	7	a	38.05	6.33	6.14	6.14	366	38.09	6.37	6.60	6.15	417
		b					335	38.1	6.34	6.68	6.15	447/439
2	1		37.99	5.94	5.84	6.10	343	38.15	5.98	6.10	6.10	459
	3		37.98	6.37	6.39	6.09	422	38.07	6.65	6.44	6.11	434
3	2	a	38.03	6.00	5.98	6.09	300	38.07	6.08	6.68	6.08	481
		b					338	38.08	6.04	6.28	6.11	445/435

Table 2. Bader atomic charges for zirconium (Zr), ligand carbons (C, C’) and average Cp carbon charge (Cp $\bar{C}$) for starting and intermediate zirconocene molecules compared to their decomposition energies. Class 1 refers to alkyl ligands, class 2 is -OH substituents, and class 3 are -NH2 ligands.

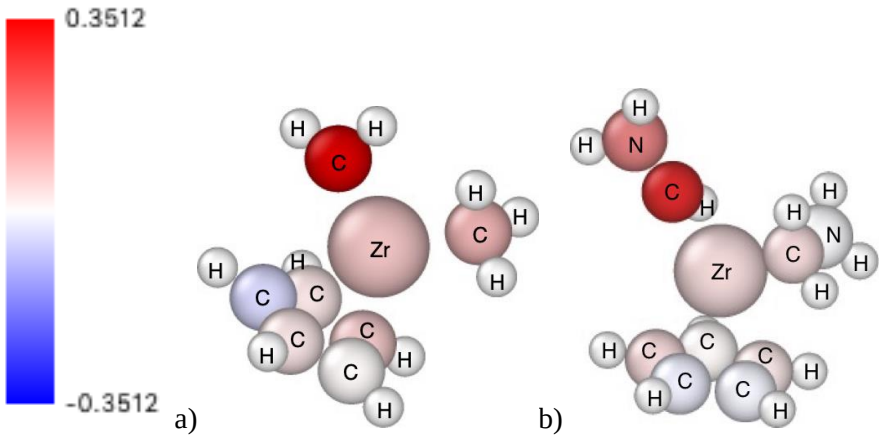

Figure 9. Bader atomic charge difference (e^-) between the reactant and intermediate projected on the intermediate for reaction 1.1 and 3.2 projected on to the intermediate. Red denotes charge gain and blue denotes charge depletion.

Class	Number		Rxn 1 Δe^-				ΔE_1(kJ/mol)	Rxn 2 Δe^-			ΔE_2 (kJ/mol)
			Zr	C	C’	Cp $\bar{C}$		Zr	C	C’	
1	1		0.08	0.35	0.10	0.02	410	0.37	-0.06	0.20	434
	2	a	0.14	0.32	0.04	0.00	373	0.27	0.00	0.36	453
		b	0.06	0.34	0.10	0.02	404	0.42	-0.08	0.39	422
		c						0.37	-0.03	0.23	416
	7	a	0.08	0.29	0.04	0.00	366	0.30	0.11	0.27	417
		b	0.09	0.37	0.00	0.00	335	0.46	0.18	0.15	447
		c						0.31	-0.03	0.28	439
2	1		0.16	0.27	0.05	0.00	343	0.26	-0.04	0.32	459
	3		0.09	0.27	0.05	0.02	422	0.34	-0.02	0.21	434
3	2	a	-0.05	0.05	0.30	0.01	300	0.31	0.31	-0.05	481
		b	-0.05	0.05	0.30	0.01	338	0.26	0.35	0.45	445
		c						0.31	0.31	-0.05	435

Table 3. Bader atomic charge changes for zirconium (Zr), ligand carbons (C, C’) and average Cp carbon charge (Cp $\bar{C}$) for starting and intermediate zirconocene molecules compared to their decomposition energies. Class 1 refers to alkyl ligands, class 2 is -OH substituents, and class 3 are -NH2 ligands.

Table 2 presents the calculated Bader charges for selected zirconocene molecules and Table 3 reports the changes in Bader charge differences associated with their respective reactions. The charges are reported for the zirconium center (Zr), the generalized carbon ligands C and C’, as well as the average Cp carbon charges, denoted as $\bar{C}$. The observed trends indicate that increasing the alkyl chain lengths leads to a rise in the charge on the zirconium atom and an increase in the average charge on the carbon atoms bound to zirconium. This phenomenon can be attributed to the electron-withdrawing effects of the additional alkyl groups. Moreover, the addition of alkyl groups to the Cp ligand results in an increase in electron density on the Cp itself. Conversely, the introduction of functional groups such as -OH or -NH_2 to the alkyl ligand withdraws charge from the zirconium-bound carbon, although it has a negligible impact on the charges of the zirconium or the carbon atoms in the Cp ligand. These trends are consistent across the intermediate complexes as well. When a Cp ligand is removed, there is an increase in charge on both the zirconium and the carbon atoms of the remaining ligands, while the average charge on the carbon atoms of the remaining Cp remains largely unchanged. Generally, compounds exhibiting the lowest average charges on zirconium and the ligand carbons correlate with lower decomposition energies. The additional charge results from the loss of a Cp ligand and the formation of an sp^2 carbon, stabilizing the intermediate complex. Consequently, the increased charge on the zirconium and the remaining Cp leads to a higher energy requirement for the formation of the final zirconium product.

This phenomenon is further illustrated in Table 3 and Figure 9, which presents the changes in Bader electron counts for each reaction. The removal of one Cp molecule from the zirconocene has minimal impact on the remaining Cp ligand. However, there is an increase in the charge on the zirconium atom and the carbon atoms bound to zirconium, with the most significant change observed in the newly formed sp^2 carbon atoms. Generally, the decomposition energy for the first reaction step decreases proportionally to the change in charge. As the reaction progresses from the intermediate to the final product charge transfers to the zirconium atom. Similar to the first reaction step, the charge on the newly formed sp^2 carbon increases, while charge is depleted from the initially formed sp^2 carbon. However, charge transfer is not the only factor that contributes to changing decomposition energies. The reactions involving the methylamine ligand have the same charge transfer for each pathway, but different decomposition energies. This suggests that while charge dynamics play a role in the reactivity of zirconocene complexes, other factors may also significantly influence the overall reaction pathway and energetics.

Discussion

Generally, the addition of larger ligands to either the zirconium center or the Cp ligand results in decomposition energy reduction. The only exception to this trend is the incorporation of a carboxylic acid into the Cp ligand, which stabilizes the initial zirconocene complex. While the presence of larger ligands lowers the decomposition energy by stabilizing the intermediate decomposition products, this stabilization leads to an increase in the decomposition energy required for subsequent reaction steps. This effect is particularly pronounced with the dimethylalcohol ligand, which decreases the energy of the first decomposition reaction by 134 kJ/mol, however, this reduction comes at the cost of increasing the energy of the second decomposition step by 75 kJ/mol.

The most significant decrease in decomposition energy was observed with modifications to the zirconocene ligand rather than the Cp ligand. The results align with the expected behavior of electron-withdrawing groups, specifically, the charge on the alkyl carbon atoms bonded to zirconium decreases in accordance with the strength of the electron-withdrawing substituents. Upon the removal of a Cp ligand, the charge on both methyl carbons increases with greater charge increase on the sp^2 carbon. Notably, the charge on the zirconium metal atom is higher when electron-withdrawing groups are present compared to systems with only methyl groups.

While thermal effects are not quantitatively analyzed in this study, it is important to note that the $-T\Delta S$ contribution to the Gibbs free energy will drive the decomposition of zirconocene to form ZrC at elevated temperatures. We can qualitatively assess the influence of thermal entropy by examining changes in molecular vibrational modes. Dichloro-zirconocene exhibits 63 vibrational modes, and substituting chlorine for alky ligands will increase the number of vibrational modes. In contrast, the Cp ligand has 34 vibrational modes. Consequently, the total number of vibrational modes—and thus the associated entropy—increases upon the decomposition of zirconocene complexes. Therefore, the thermal contributions are expected to be amplified as the ligand size grows and increase the reactivity differences and stability between dimethyl-zirconocene and complexes with larger ligands. This suggests that, while the focus of this study is on the electronic factors influencing decomposition, changes in thermal contributions from ligand size will also play a significant role in the overall energetics.

Larger ligand sizes generally decrease the decomposition energy of zirconocene complexes; however, this reduction often comes at the cost of stabilizing the intermediate complexes and introducing competing reaction pathways can lead to distinct overall mechanisms for ZrC surface

deposition and impact the growth of ZrC monolayers, as well as the influence of non-alkyl substituents on surface characteristics, remains to be explored and validated through experimental studies. Future research will be essential to elucidate these relationships and provide insights into the mechanisms governing ZrC surface growth.

We explored how ligand selection influences the decomposition energy of zirconocene molecules in the context of chemical vapor deposition (CVD) for zirconium carbide (ZrC) coatings. Density-functional theory (DFT) calculations reveal that the introduction of electron-withdrawing groups to the zirconocene ligand has a more pronounced effect on reducing decomposition energy compared to modifications made to the aromatic cyclopentadienyl (Cp) ligand. The electron-withdrawing groups stabilize the intermediate products, which decreases removal of one Cp, while increasing the energy to remove the second Cp. Overall, this results in lower decomposition energies. Furthermore, the presence of larger ligands introduces additional decomposition pathways, which may yield a variety of deposited products. Research into the effects of different non-alkyl ligands on CVD processes is ongoing, and further investigations will be essential to fully understand their impact on the deposition and properties of ZrC coatings.

Findings and Conclusions

We have successfully synthesized and crystallographically characterized several small molecule zirconium and hafnium precursors which are not available through commercial vendors. These starting materials have been processed by MOCVD in a custom-built CVD system which has demonstrated volatility and deposition of ceramic material. Both zirconium and hafnium have been observed deposited on the silicon substrates (depending on the identity of the starting material). Importantly, no deposition was observed when dimethyl bis(pentamethylcyclopentadienyl) zirconium (IV) was processed under our conditions, highlighting the importance of the ligand system on the volatility and deposition of molecular precursors. In addition to experimental efforts, theoretical modeling was used to build a library of relevant zirconocene precursors and evaluate the decomposition pathways present for those precursors towards zirconium carbide. It was determined that larger, bulkier ligands provide a robust stabilization of the decomposition pathway, allowing for more readily processable materials. Finally, our team has procured and stood up advanced CVD capabilities in the form of a plasma – enhanced CVD system, this will allow for optimization of the processing conditions to generate thin films of ceramic.

References

(1) Blum, V.; Gehrke, R.; Hanke, F.; Havu, P.; Havu, V.; Ren, X.; Reuter, K.; Scheffler, M. Ab initio molecular simulations with numeric atom-centered orbitals. *Comput. Phys. Commun.* 2009, *180* (11), 2175−2196.

(2) Havu, V.; Blum, V.; Havu, P.; Scheffler, M. Efficient O(N) integration for all-electron electronic structure calculation using numeric basis functions. *J. Comput. Phys.* 2009, *228* (22), 8367−8379.

(3) Marek, A.; Blum, V.; Johanni, R.; Havu, V.; Lang, B.; Auckenthaler, T.; Heinecke, A.; Bungartz, H. J.; Lederer, H. The ELPA library: scalable parallel eigenvalue solutions for electronic structure theory and computational science. *J. Phys.: Condens. Matter* 2014, *26* (21), No. 213201, DOI: 10.1088/0953-8984/26/21/ 213201.

(4) Ren, X.; Rinke, P.; Blum, V.; Wieferink, J.; Tkatchenko, A.; Sanfilippo, A.; Reuter, K.; Scheffler, M. Resolution-of-identity approach to Hartree−Fock, hybrid density functionals, RPA, MP2 and GW with numeric atom-centered orbital basis functions. *New J. Phys.* 2012, *14* (5), No. 053020.

(5) Becke, A. D. Density-functional thermochemistry. III. The role of exact exchange. J. Chem. Phys. 1993, 98, 5648−5652.

(6) Johnson, E. R.; Becke, A. D. A post-Hartree-Fock model of intermolecular interactions: inclusion of higher-order corrections. *J. Chem. Phys.* 2006, *124*, 174104.

(7) Johnson, E. R.; Becke, A. D. A post-Hartree-Fock model of intermolecular interactions. *J. Chem. Phys.* 2005, *123*, 024101.

(8) Becke, A. D.; Johnson, E. R. Exchange-hole dipole moment and the dispersion interaction. *J. Chem. Phys.* 2005, *122*, 154104.

(9) Havu, V.; Blum, V.; Havu, P.; Scheffler, M. Efficient O(N) integration for all-electron electronic structure calculation using numeric basis functions. *J. Comput. Phys.* 2009, *228* (22), 8367−8379.

(10) Ren, X.; Rinke, P.; Blum, V.; Wieferink, J.; Tkatchenko, A.; Sanfilippo, A.; Reuter, K.; Scheffler, M. Resolution-of-identity approach to Hartree−Fock, hybrid density functionals, RPA, MP2 and GW with numeric atom-centered orbital basis functions. *New J. Phys.* 2012, *14* (5), No. 053020.

(11) Otero-de-la-Roza, A.; Johnson, E. R.; Luaña, V. Critic2: A program for real-space analysis of quantum chemical interactions in solids. *Comput. Phys. Commun.* 2014, *185*, 1007−1018.

(12) Yu, M.; Trinkle, D. R. Accurate and efficient algorithm for Bader charge integration. *J. Chem. Phys.* 2011, *134*, 064111.

(13) Diana, E.; Rossetti, R.; Stanghellini, P. L.; and Kettle, S. F. A. Vibrational Study of (η5-Cyclopentadienyl) metal Complexes. *Inorganic Chemistry* **1997** *36* (3), 382-391 DOI: 10.1021/ic960545n

Acknowledgement/Disclaimer

This work was sponsored by the Office of Naval Research (ONR), under grant (or contract) number N0001424IP00028-Sandia Proposal 018200129. The views and conclusions contained herein are those of the authors only and should not be interpreted as representing those of ONR, the U.S. Navy or the U.S. Government.

Sandia National Laboratories is a multimission laboratory managed and operated by National Technology & Engineering Solutions of Sandia, LLC, a wholly owned subsidiary of Honeywell

International Inc., for the U.S. Department of Energy's National Nuclear Security Administration under contract DE-NA0003525.

Appendix A: Supplementary information

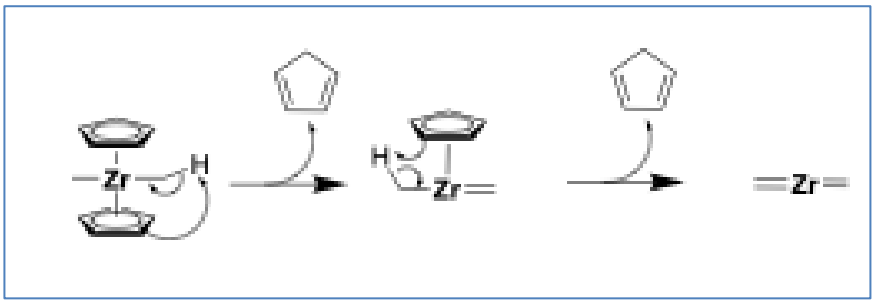

Figure 10. Decomposition mechanism of **1.1**.

a)

b)

c)

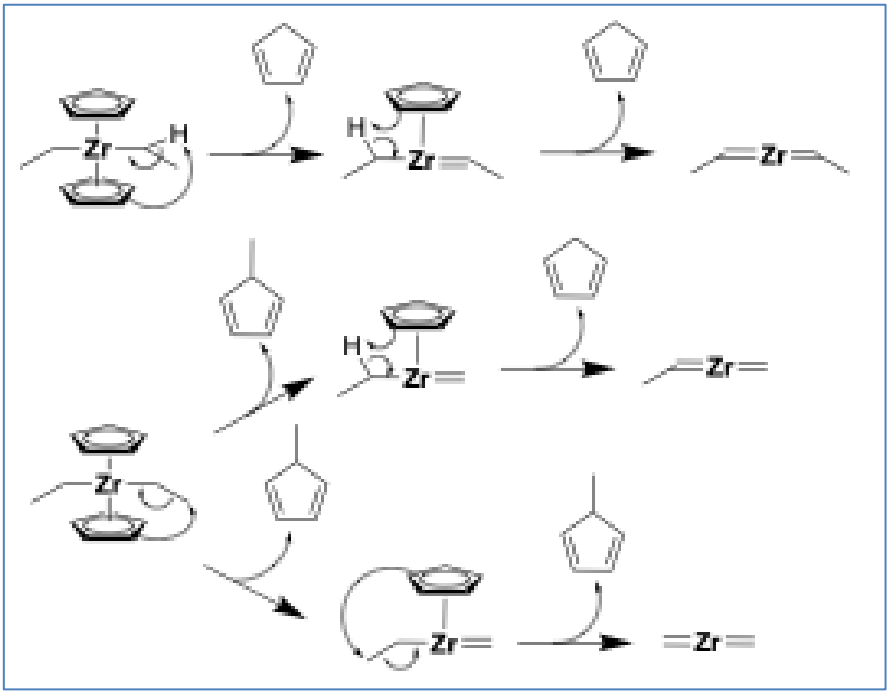

Figure 11. Decomposition mechanisms of **1.2**.

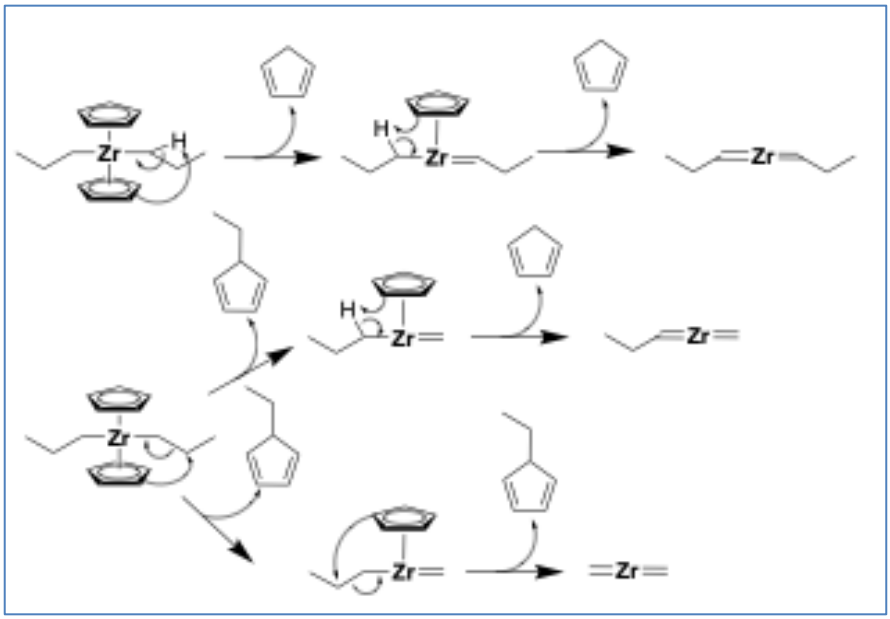

Figure 12. Decomposition mechanisms of **1.3**.

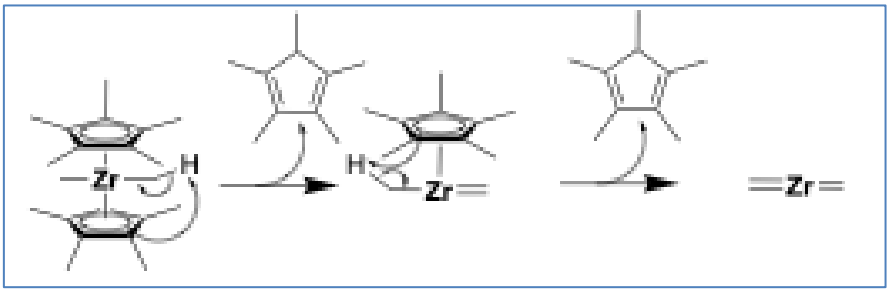

Figure 13. Decomposition mechanisms of **1.4**.

a)

b)

c)

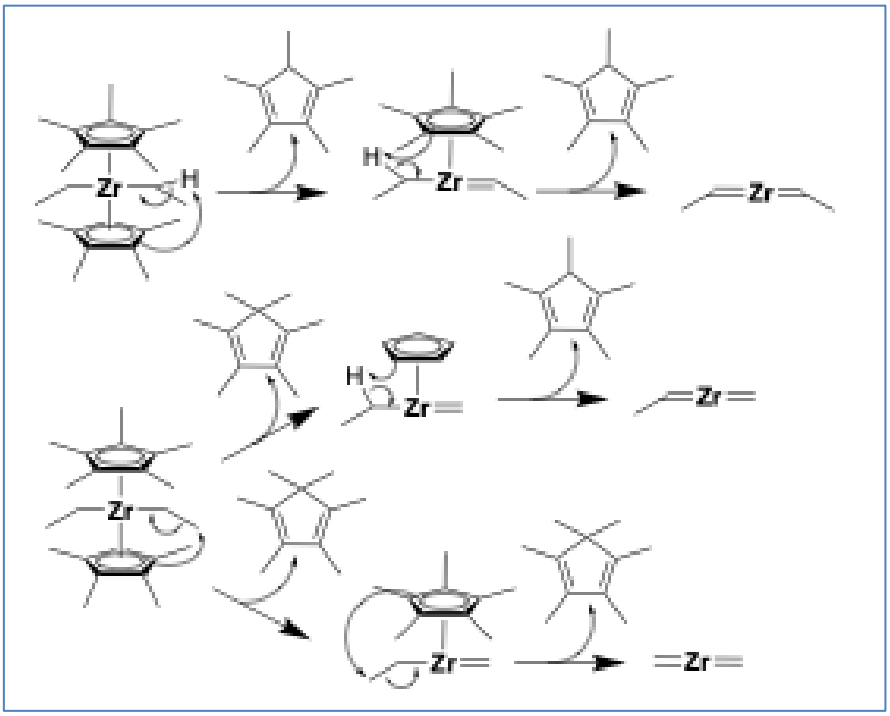

Figure 14. Decomposition mechanisms of **1.5**.

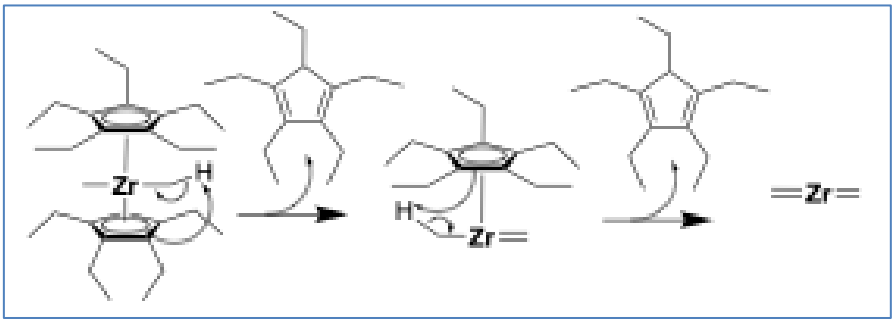

Figure 15. Decomposition mechanisms of **1.6**.

a)

b)

c)

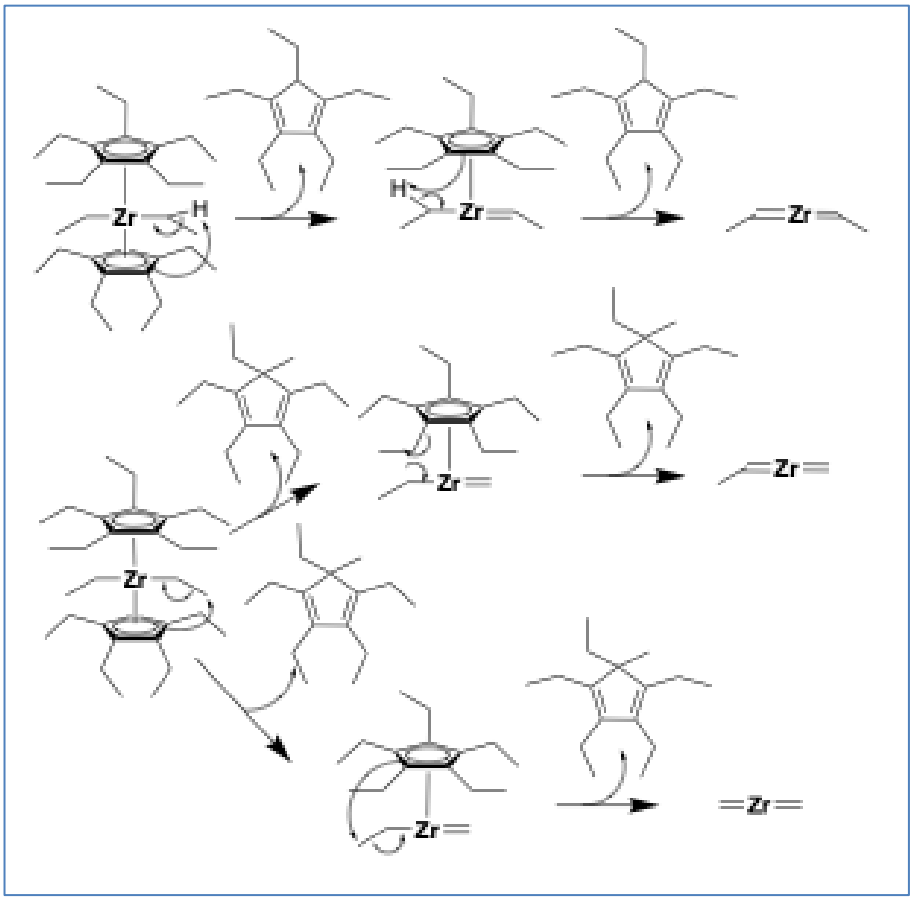

Figure 16. Decomposition mechanisms of **1.7**.

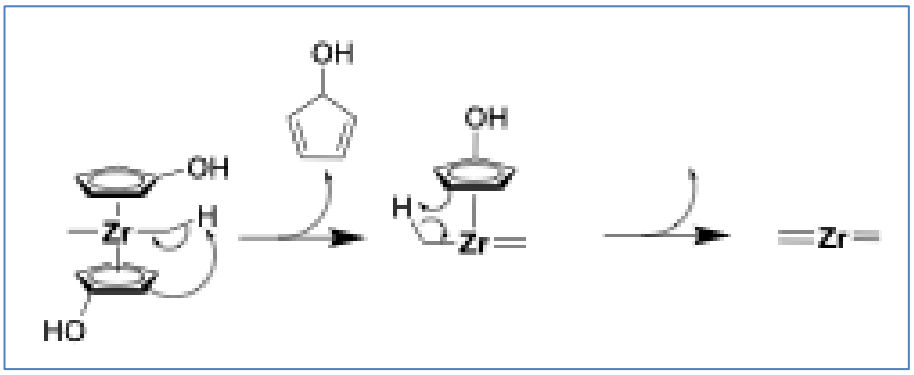

Figure 17. Decomposition mechanisms of **2.1**.

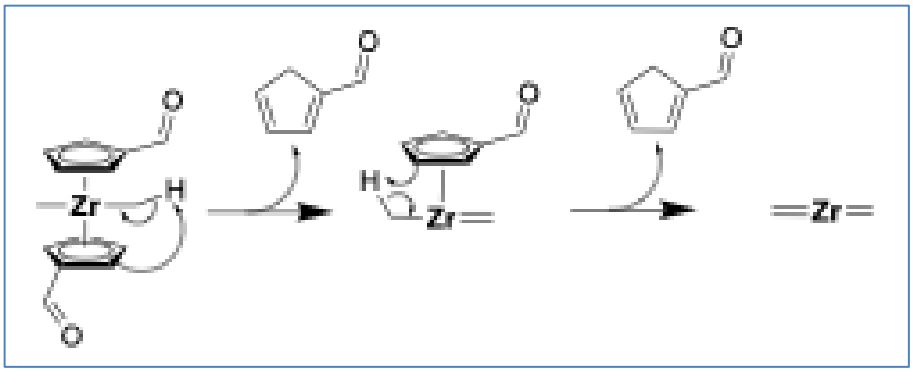

Figure 18. Decomposition mechanisms of **2.2**.

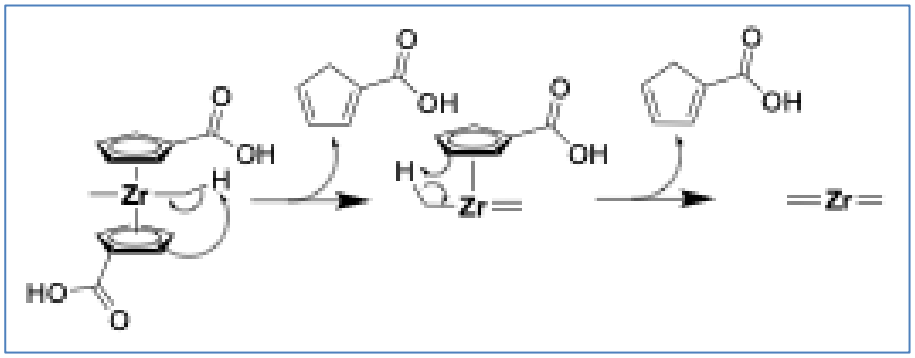

Figure 19. Decomposition mechanisms of **2.3**.

a)

b)

c)

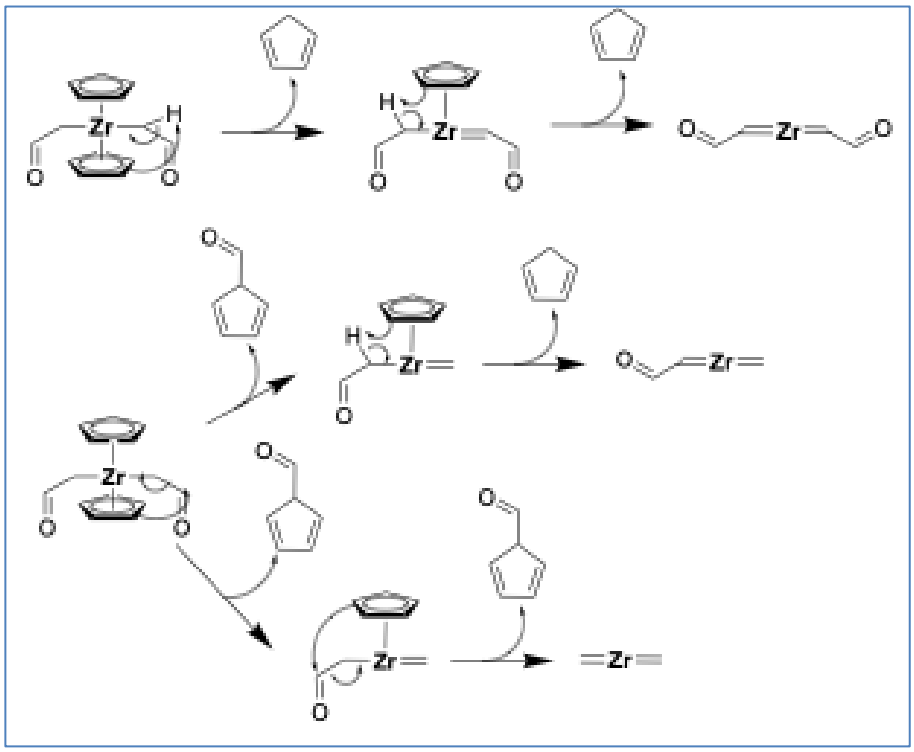

Figure 20. Decomposition mechanisms of **2.4**.

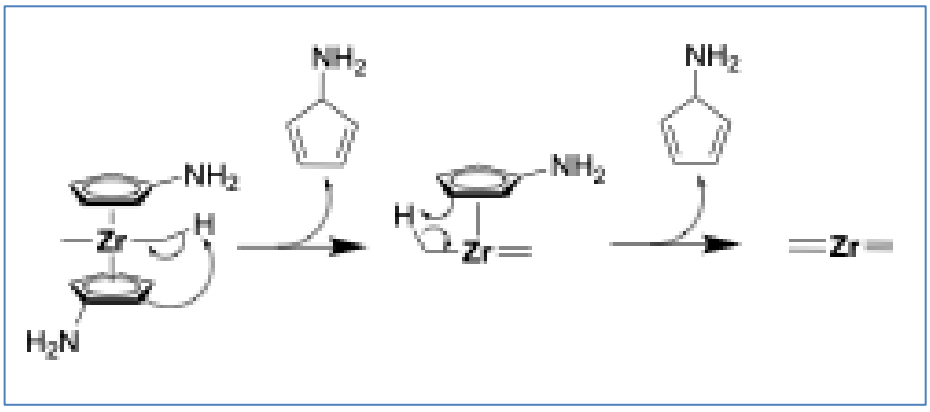

Figure 21. Decomposition mechanisms of **3.1**.

a)

b)

c)

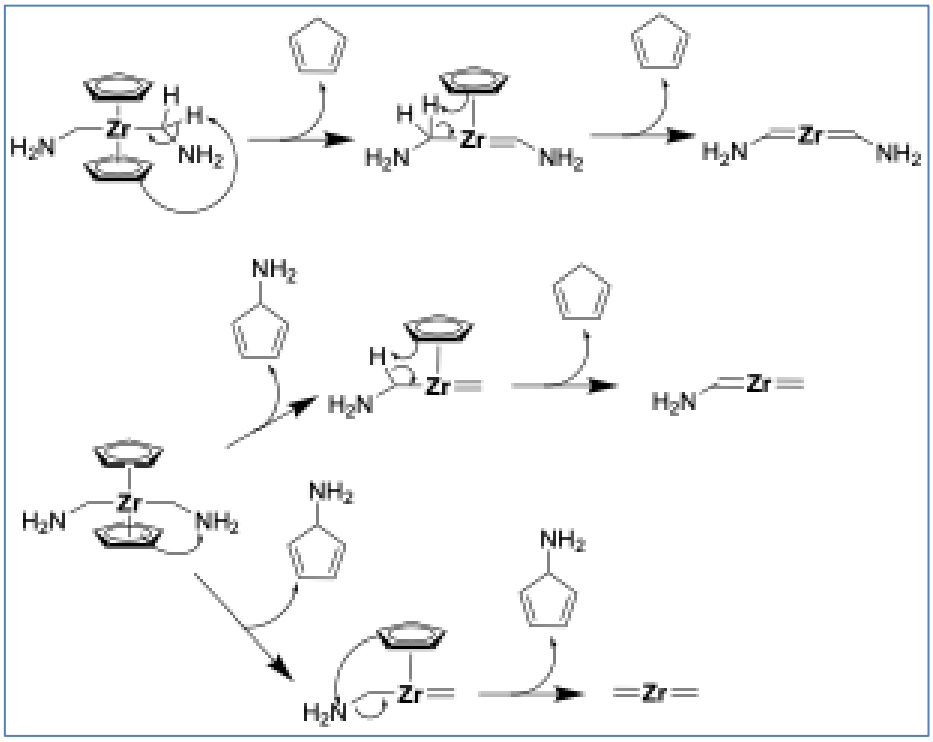

Figure 22. Decomposition mechanisms of **3.2**.